Strong variation of the phase lag in the vicinity of autoionizing resonances

Rekishu Yamazaki and D. S. Elliott*
School of Electrical and Computer Engineering and Department of Physics, Purdue University, West Lafayette, Indiana 47907, USA
(Received 11 September 2007; published 5 November 2007)

We have observed the phase lag in the sinusoidal variation of the asymmetric photoelectron angular distributions into two ionization channels of atomic barium using an ω-2ω excitation scheme. We excite atomic barium from the $6s6p\ ^1P_1$ intermediate state electron to an energy between the $5d_{3/2}\epsilon$ and the $5d_{5/2}\epsilon$ thresholds with concurrent one-photon and two-photon interactions. The left-right asymmetry of the photoelectron angular distributions for the two energy-resolved product states, $6s_{1/2}\epsilon$ and $5d_{3/2}\epsilon$, show sinusoidal modulation as a function of the relative phase of the ω-2ω fields. The phase difference between these signals, or phase lag, varies rapidly with the laser frequency when the interaction is nearly resonant with autoionizing resonances in the continuum. An exceptionally large phase lag variation of over 2π was measured.

DOI: 10.1103/PhysRevA.76.053401 PACS number(s): 32.80.Qk, 32.80.Dz, 32.80.Fb

I. INTRODUCTION

Since the first demonstration of product state control, performed by Zhu *et al.* on photodissociation of HI [1], the phase shift between the sinusoidally varying product state probabilities has been the subject of numerous studies [2–13]. This first example of control was achieved through a multipathway excitation scheme, where two photodissociation continua were excited by two coherent excitation pathways: three-photon absorption of a field at frequency ω; and linear absorption of a field at frequency 3ω. As a result of an interference between these two pathways, sometimes referred to as ω-3ω interference, the excitation probabilities for each product channel showed sinusoidal modulation as the relative phase difference between the two excitation pathways was varied continuously. These authors noted a phase difference between the modulation of the signals for these two channels, which they termed the "phase lag." They observed a phase lag of up to 150° between the sinusoidal probabilities of product states, stimulating discussion of the idea of *optimization* in the product state control. Optimization can be achieved by causing the phase lag to be π, yielding a maximum for one product when the other is minimized, and vice versa. In 1997, Zhu *et al.* [2,3] reported observing a large variation of the phase lag for photodissociation of HI and DI, ranging from 40° to 170°, and varying with the wavelength of the exciting laser fields. They suggested that the control of the phase lag was due to the resonance structure in the excited continuum region.

A number of theoretical investigations into the origin and properties of the phase lag have been reported [2,4–12]. Fiss and co-workers [2,4] and Lambropoulos and Nakajima [5] showed that the dominant factor for the origin of the phase lag is the coupling of two or more continua to a resonance, such as an autoionizing or predissociating resonance. These studies showed a clear theoretical development of the variation of the phase lag from resonance structures in the continuum. Lambropoulos and Nakajima also showed that the phase lag is a more general phenomenon than originally considered, and that it should be expected in atomic as well as molecular systems. While these studies clearly predict the role of the resonance effects, quantitative comparison between experiment and theory is lacking, perhaps due to the high density of resonances and the complexity in the calculations of these effects for even the simplest molecular system used in the experimental demonstrations.

In a recent Letter [13], we reported measurements of the phase lag between photoionization channels of atomic barium. We carried out these measurements using ω-2ω interference, i.e., two-photon ionization with a field at frequency ω and linear absorption of its second harmonic, resulting in asymmetric photoelectron angular distributions. We performed the experiment in the vicinity of the autoionizing resonances converging upon the $5d\ ^2D_{5/2}$ threshold in atomic barium. By working with an atomic system in a spectral region where the resonance structures are well resolved, we expect the results of our measurements to form the basis for quantitative tests of the theory of the phase lag. In the present paper, we provide a full account and analysis of these observations.

II. EXCITATION SCHEME AND EXPERIMENT

We show a schematic diagram of the relevant energy levels of atomic barium and the excitation scheme used for the experiment in Fig. 1. We tune the frequency ω_0 of the first laser to near resonance with the $6s^2\ ^1S_0 \rightarrow 6s6p\ ^1P_1$ transition, at a wavelength λ_0 of approximately 554 nm. We excite the $6s6p\ ^1P_1$ atoms to a continuum state of energy in the range $\epsilon = 46\,908 - 47\,709\ \mathrm{cm}^{-1}$, i.e., in the region between the $5d\ ^2D_{3/2}$ and $5d\ ^2D_{5/2}$ (abbreviated $5d_{3/2}$ and $5d_{5/2}$, respectively) thresholds, via two excitation pathways: (1) two-photon excitation of the atom driven by a coherent laser field at frequency ω_1 (wavelength $\lambda_1 \sim 686$ nm), and (2) linear excitation by a laser field component of frequency $\omega_2 = 2\omega_1$ (wavelength $\lambda_2 \sim 343$ nm). The discrete structures in these continuum regions have been studied extensively [14,15]. The electron is coupled to different continuum channels: the $6s\ ^2S_{1/2}$ (which we will abbreviate as $6s_{1/2}$) core state plus a photoelectron with kinetic energy of about 0.6 eV; and the $5d_{3/2}$ core state with a 0.04 eV kinetic energy photoelectron.

*elliottd@purdue.edu

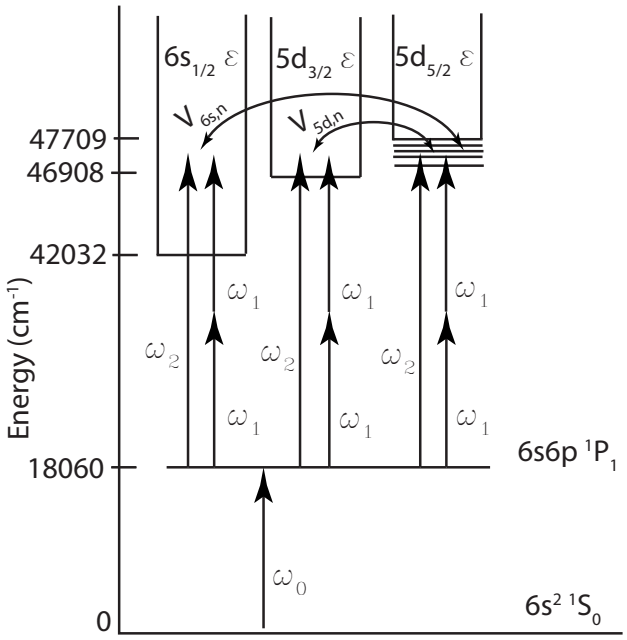

FIG. 1. Energy level diagram of barium showing the relevant transitions in the experiment. The ω_2 beam is the phase-coherent second harmonic of the laser fundamental at frequency ω_1. The excited electrons couple to two ionization channels, resulting in photoelectrons with different kinetic energies of 0.6 eV (fast) or 0.04 eV (slow).

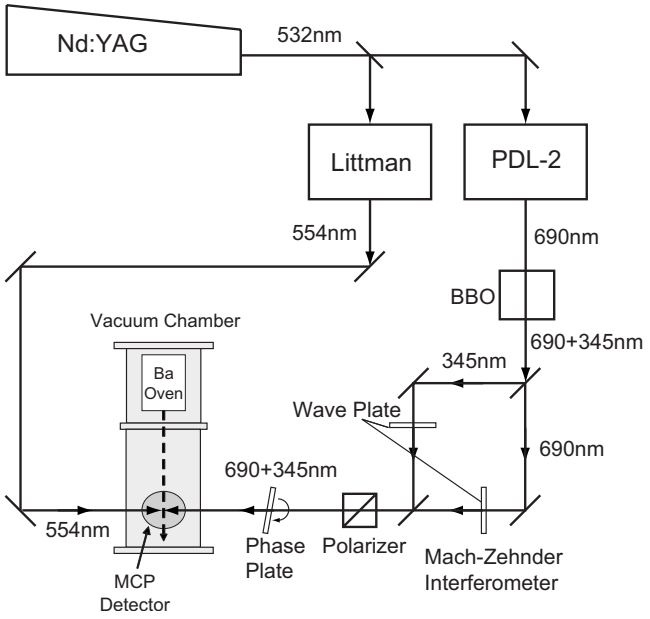

FIG. 2. Experimental setup. Two dye lasers, labeled Littman and PDL-2, pumped with a Q-switched Nd:YAG laser, and a nonlinear crystal (BBO) are used to generate the laser beams with frequencies $\omega_{0,1,2}$. The relative optical phase between ω_1 and ω_2 is varied with a rotatable fused silica plate controlled with a stepper motor. The atom beam is generated in an effusive oven inside the vacuum system, and propagates in a direction perpendicular to the laser beams. The photoelectrons are detected with the MCP and phosphor screen detector assembly and the electron images formed on the screen are captured with a CCD camera and stored in a laboratory PC.

We call these electrons the fast and slow electrons, respectively. Since two coherent excitation pathways from the intermediate excited state involve even and odd photon numbers, these two pathways couple to continua with different parity; therefore the resulting photoelectron angular distributions (PAD) from the two-pathway interference exhibit an asymmetry for each product channel [16–22]. Our phase lag studies are based upon the variation of these photoelectron angular distributions.

We show a schematic diagram of the experimental setup in Fig. 2. Two dye lasers are pumped with the second harmonic (532 nm) output of a Q-switched neodymium-doped yttrium aluminum garnet (Nd:YAG) laser. The duration, pulse repetition rate, and typical pulse energy of the output of the Nd:YAG laser are ~10 ns (full width at half maximum), 10 Hz, and 80 mJ, respectively. The first dye laser, a Littman-type home-made laser, generates the output pulse at frequency ω_0 with an energy of 200 μJ. We hold the output frequency of this laser fixed at the $6s^2\ ^1S_0 \rightarrow 6s6p\ ^1P_1$ resonance during the experiment. We spatially filter this horizontally polarized beam to restrict the transverse mode to a nearly Gaussian profile, and focus it onto the interaction region with a beam radius w_0 (the radius at which the intensity decreases to e^{-2} of its on-axis value) of approximately 300 μm at the interaction region. Using a neutral density filter, we adjust the pulse energy of this beam at the interaction region to <50 μJ to avoid three-photon ionization of the ground state.

The second dye laser, a Spectra Physics PDL-2, produces the ω_1 pulse at an output wavelength of around 686 nm, with a typical laser pulse energy of 4 mJ. We tune the wavelength of this laser using a stepper motor attached to the diffraction grating inside the oscillator cavity, with a step size of 0.0030 nm at 690 nm (0.063 cm^{-1}). We generate the phase-coherent uv pulse ($\omega_2=2\omega_1$) through second-harmonic generation of the ω_1 beam using a type-I phase-matched β–barium borate (BBO) nonlinear crystal.

We separate the ω_1 and ω_2 beams along the two arms of a Mach-Zehnder interferometer in order to individually adjust their polarization and beam overlap. We mount the interferometer on rubber vibration-damping pads and enclose it in a Plexiglas box to minimize fluctuations in the relative path length due to mechanical vibrations and air flow. A polarizer positioned after the final reflector of the interferometer, on which the beams are recombined, improves the polarization of the beams, and also allows us to control the power of each beam (by adjusting the wave plate inserted in each arm of the interferometer).

A 1-cm-thick rotatable fused silica window functions as an optical phase shifter [22,23]. The rotation angle of the plate was adjusted by a stepper motor, with a step size of 0.0016 deg/step, controlled by a laboratory computer and LABVIEW interface. The typical range of rotation used during an experiment was 1.5° at 16° from normal incidence, varying the relative phase $\Delta\phi=\phi^{\omega_2}-2\phi^{\omega_1}$, where ϕ^{ω_1} and ϕ^{ω_2} are the phases of the fundamental (ω_1) and harmonic (ω_2)

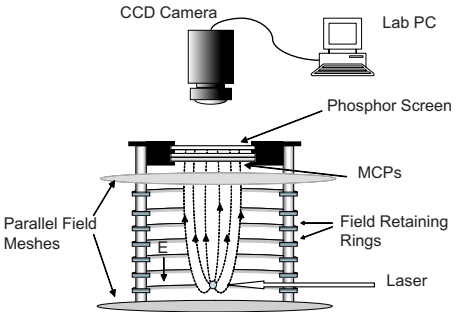

FIG. 3. (Color online) Photoelectron imaging detector assembly used in the experiment. Photoelectrons ejected from the laser-atom interaction are accelerated toward the MCP detector assembly by the uniform dc electric field generated by the biased parallel field meshes. The electron image formed on the phosphor screen is captured using a data acquisition system, consisting of a CCD camera and a frame grabber interface card in the laboratory PC.

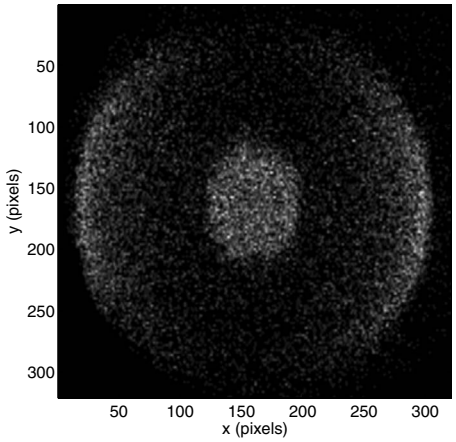

FIG. 4. Typical photoelectron image recorded during the experiment. The larger (smaller) ring in the figure is the maximum radius traveled by the fast (slow) electrons. The laser beams travel in the $\pm y$ directions, while the polarization of the laser fields is set to the x direction. The image shown is a convolution of a raw data image with a 2×2 window function to improve the image visibility.

fields, respectively, by about 16 rad. We calibrated the relative optical phase $\Delta\phi$, which changes nonlinearly with the window rotation angle, by placing a second BBO crystal after the rotating window and observing the optical interference between the ultraviolet beams generated in the first and second BBO crystals. We calculate that the transverse displacement of the two beams as the window rotates over this range is 3 μm, negligible in comparison to any of the beam radii inside the vacuum chamber. These beams propagate in the interaction region in a direction counter to that of the 554 nm laser beam.

The pulse energies of the 343 and 686 nm beams are 7 μJ and 2 mJ, respectively, at the interaction region, chosen so as to make both ionization signals observable and of comparable magnitude. These beams have nearly Gaussian transverse profiles, although the uv beam is elliptical due to phase-matching effects in the BBO crystal. The radius w_0 of the red beam is about 290 μm, while that of the uv beam is 220 μm$\times$510 μm. We control the relative timing between the 554 nm laser pulse and two-color pulse by varying the optical path lengths, which we adjust such that the peaks of the laser intensity coincide at the interaction region. The atom beam is generated in a hot effusive oven inside the vacuum chamber. The background pressure inside the vacuum chamber is 2×10^{-8} torr. We estimate the atom density of the barium at the interaction region to be 4.3×10^{7} cm^{-3} for a typical oven operating temperature of 650 °C. The atom beam is collimated through a pinhole to a diameter of $\sim$1 mm at the interaction region and propagates in a direction perpendicular to the laser beams.

We observe the photoelectrons ejected from the laser-atom interaction using a detector that consists of a microchannel plate (MCP) electron multiplier and a phosphor screen, similar to that reported by Helm *et al.* [24]. We show a schematic diagram of the photoelectron detector system in Fig. 3. The details of our photoelectron detection system as well as the image processing are described elsewhere [25] and we explain only briefly here. The photoelectrons ejected through the interaction travel through a flight region, where a constant, uniform electric field is maintained with a pair of parallel meshes to which we apply a typical potential difference of 120 V. We cancel the Earth's magnetic field using three orthogonal pairs of magnetic field coils to less than 10 mG throughout the flight region. The photoelectrons follow parabolic trajectories as they accelerate toward the MCP electron multiplier, where they are amplified, and, upon striking the phosphor screen, produce a spot of light. A charge-coupled device (CCD) camera acquires the image of the phosphor screen for each laser pulse, which is stored in a laboratory computer (PC). A typical number of electrons observed on the detector is 60–180/pulse and we accumulate images from 1000–3000 pulses to obtain a smooth image. In order to reduce the false counting of the electron image, we employ an above-threshold detection algorithm to process each image [26].

We show a typical photoelectron image recorded with this detector system, accumulated after only 100 laser pulses, in Fig. 4. The dimension of each pixel of this image scales to 100 μm in the plane of the photoelectron detector phosphor screen. During the experiment, all the laser beams propagate in the $\pm y$ directions of the figure and the polarization of all the beams is set to the x direction. The two rings in the image correspond to the maximum radius traveled for the two different electron kinetic energies, i.e., the fast and slow electrons. The fast electrons, with the higher kinetic energy, create a larger ring, while the slow electrons form the much smaller ring.

We use these images to carry out three sets of measurements.

(1) We measure the single-pathway noninterfering energy-resolved spectra of the autoionizing resonances in the energy region of interest. We obtain the electron counts for fast and slow electrons by summing up the appropriate regions of the image. Inside the smaller ring, where the images of the two electron products overlap, we extract the slow-electron signal by smoothly extending the fast-electron counts through this region of the detector.

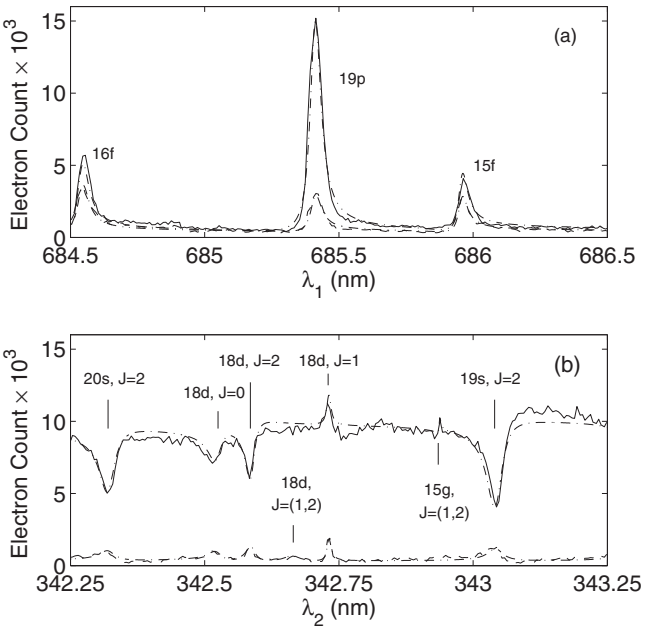

FIG. 5. Autoionization spectra. The plots correspond to (a) $5d\,^2D_{5/2}nl[3/2]$ peaks excited through two-photon interaction with the red beam of wavelength λ_1; and (b) $5d\,^2D_{5/2}nl,J$ resonances excited through linear absorption of the uv beam of wavelength $\lambda_2=\lambda_1/2$. In each, the solid line shows the fast-electron spectrum, while the dashed line shows the slow-electron spectrum. The dot-dashed lines are the results of a fit of Eq. (1) to the measured spectra, used to obtain the autoionization parameters such as q, Γ, D, and V. Peaks are identified through comparison with the work of Refs. [14] (red spectra) and [15] (uv spectra).

(2) We analyze these images to obtain the single-pathway noninterfering energy-resolved photoelectron angular distribution, using an inversion method discussed in Ref. [27].

(3) For the case of two-pathway excitation, we analyze images like those of Fig. 4 to determine the left-right asymmetry introduced by the interference.

The primary source of noise in the images is shot noise associated with counting discrete photoelectrons. The noise generated from scattered light or background gas ionization by the 554 and 686 nm laser pulses is less than 1 count/shot, while the background noise from the ultraviolet pulse was about 13 counts/shot, uniformly distributed across the MCP detector.

III. RESULTS

A. Single-pathway autoionizing resonance spectroscopy

In order to characterize the autoionizing resonance (AIR) structures in the region of interest, we first measured the single-pathway noninterfering spectrum for each excitation pathway (i.e., two red photons or one uv photon) from the $6s6p\,^1P_1$ intermediate state in the complete region between the $5d_{3/2}$ and $5d_{5/2}$ thresholds ϵ=46 908 and 47 709 cm^{-1}, respectively. Using these initial spectra, we narrowed our interest to the region between 47 193 and 47 278 cm^{-1} for our detailed measurements. In this spectral region, the AIR peak spacings are much larger than the spectral linewidths, and the kinetic energy of the slow electrons is sufficiently large to create a resolvable image on the MCP detector.

We show the product-resolved AIR structures for each excitation pathway as a function of wavelength in Fig. 5. The two-photon ionization spectra in Fig. 5(a) show strong AIR peaks with nearly symmetric profiles, while the one-photon ionization spectra, in Fig. 5(b), show highly asymmetric profiles as well as window resonances, the signatures of a strong interference between the direct ionization and the ionization from the decay of autoionizing states.

In order to estimate the effect of the autoionizing resonances on the variation of the phase lag, it is necessary to parametrize the line shapes for the individual processes. We therefore fit the measured line shapes to the form

$$R_f^{(M)} = 2\pi \int dt\, f(t) \left| D_{fi}^{(M)} + \sum_n \frac{V_{fn}\Omega_n^{(M)}(1 - i/q_n)}{(\Delta_n + i\Gamma_n/2)} \right|^2 \quad (1)$$

to obtain $D_{fi}^{(M)}$, the M-photon (where M=1 or 2) bound-free dipole matrix element coupling the initial state $|i\rangle$ to the $|f\rangle$ continuum, V_{fn}, the matrix element of the configuration interaction coupling the autoionizing state $|n\rangle$ to the same continuum, the resonant frequency of state $|n\rangle$, the asymmetry parameter q_n, and the linewidth Γ_n for each peak observed. The autoionizing resonance width is related to the coupling strengths V_{fn} through $\Gamma_n = 2\pi\Sigma_f |V_{fn}|^2$. $\Omega_n^{(M)}$ represents the M-photon Rabi frequency coupling the initial state $|i\rangle$ and the autoionizing state $|n\rangle$. Δ_n is the frequency difference between ω_2 (=$2\omega_1$) and the transition frequency to the discrete state. The time integral is over a period that includes the entire laser pulse, whose time dependence is represented by the function $f(t)$. We expect that, at the intensities used in our work, the time dependence of the various terms within the integrand are all the same, and the specific form of $f(t)$ is unimportant. We show the fitted spectra as dot-dashed lines in Fig. 5, and list all the parameters used for the fit in Tables I and II.

The fitted AIRs show very good agreement with the data for the most part. There is a slight dependence of the direct ionization parameter on wavelength for the fast electrons with the ultraviolet excitation, resulting in higher ionization yield in the higher-wavelength region compared to the lower-wavelength region. We include this in the fit. We encountered a problem in fitting the $5d\,^2D_{5/2}ns,J=2$ peaks, in that we were unsuccessful in finding an asymmetry parameter q that could fit both the fast- and slow-electron spectra. Despite the slight discrepancy on these particular resonances, the overall fitting quality of the resonances is satisfactory.

B. Single-pathway photoelectron angular distribution measurements

As a means of further characterizing the single-pathway, noninterfering interactions, we have analyzed the images produced by the imaging photoelectron detector in order to determine the photoelectron angular distributions as a function of the laser wavelength. The rapid variation of photoelectron angular distributions as a function of wavelength

TABLE I. Line shape parameters of the $5d\ ^2D_{5/2}nl[3/2]$ resonances excited through two-photon absorption of the red laser.

$D_{6s_{1/2}\epsilon}$	23.49				
$D_{5d_{3/2}\epsilon}$	21.70				
λ^*_{red} (nm)	687.00	685.96	685.41	684.54	684.10
nl	18p	15f	19p	16f	20p
E (cm^{-1})	47 172.12	47 216.49	47 239.76	47 276.69	47 295.43
q	0.36	0.89	0.69	0.78	0.86
Γ (cm^{-1})	2.02	1.76	2.07	2.17	2.06
$V\Omega_{6s_{1/2}\epsilon}$	−32.10	−25.52	−59.48	−32.69	−79.46
$V\Omega_{5d_{3/2}\epsilon}$	−11.74	−19.50	−19.87	−26.58	−26.11

when exciting into structured continua has been studied previously [28]. We describe the observed PAD in terms of the Legendre polynomials $d\sigma/d\Omega=(\sigma/4\pi)[1+\Sigma_{l=2,4,6}\beta_l \times P_l(\cos\Theta)]$, where Θ is the polar angle defined with respect to the symmetry axis parallel to the laser polarization, the x axis in our geometry. The azimuthal (Φ) dependence of PAD is understood to be uniform from the cylindrical symmetry of the experimental setup. For noninterfering interactions, the image is symmetric in x, such that β_l is zero for odd l. We show the results of the PAD measurement for two-photon excitation by the red laser in Fig. 6, and for linear excitation by the uv beam in Fig. 7. In these figures, the components shown are β_2 (○), β_4 (▽), and β_6 (×).

We measured the PAD over a wavelength range from $\lambda_1=684.5$ to 686.4 nm. This range corresponds to $\Delta n\sim 1$, where n represents the principal quantum number of the discrete series of absorption lines. The observed PAD shows visible amplitudes in β_l components up to $l=2$ (○), 4 (▽), or 6 (×), depending on the ionization channel and on the order of the interaction. It is apparent from the data that the PAD changes drastically near the AIRs for all the spectra, indicating the strong change in the outgoing electron waves around the AIRs.

Due to the large number of continuum states that can be excited through the interaction, as listed in Table III, a rigorous separation of the outgoing electronic waves using only the PAD measurements is not in general possible. The PAD measurement can, however, provide a qualitative understanding of the constituents of the outgoing electron waves. For example, two-photon excitation by the red laser excites odd-parity final states. As shown in Fig. 6, β_4 (▽) and β_6 (×) are rather small for both fast- and slow-electron channels, while β_2 (○) is strong for both channels, indicating a strong p wave for both outgoing channels. Near the $5d\ ^2D_{5/2}15f[3/2]$ and $5d\ ^2D_{5/2}16f[3/2]$ resonances, β_2 for the fast electrons gets very small as well, as the distributions are nearly isotropic. For single-photon excitation by the ultraviolet laser, even-parity final states are excited. While possible electron outgoing waves are s, d, and g waves, the magnitudes of the β_6 coefficients are very low throughout the entire range (see Fig. 7), indicating no substantial g-wave component. The fast electron signal has significant β_2 and β_4 terms, suggesting angular momentum states of the outgoing wave up to d wave, while the slow-electron channel has very little d wave. The angular distributions tend to vary quickly near some of the autoionizing resonances.

We show a summary of the general character of the outgoing electronic waves estimated from a single-pathway PAD measurement in Table III.

C. Phase lag in the asymmetric PAD measurements

When both the horizontally polarized ultraviolet and red fields are present, we observe a left-right asymmetry in both the fast- and slow-electron images due to the interference

TABLE II. Line shape parameters of the $5d\ ^2D_{5/2}nl,J$ resonances excited through linear absorption of the uv field.

$D_{6s_{1/2}\epsilon}$	98.33										
$D_{5d_{3/2}\epsilon}$	18.37										
λ^*_{red} (nm)	686.73	686.57	686.08	685.87	685.46	685.33	685.17	685.05	684.64	684.14	684.03
nl	17d	17d	19s	15g	18d	18d	18d	18d	20s	19d	19d
J	2	0	2	(1,2)	1	(1,2)	2	0	2	1	(1,2)
E (cm^{-1})	47 183.62	47 190.51	47 211.01	47 220.00	47 237.53	47 243.32	47 249.83	47 255.23	47 272.45	47 293.93	47 298.60
q	−0.72	−0.50	−0.27	1.01	0.05	−0.20	−0.40	−0.71	−0.33	0.20	−0.20
Γ (cm^{-1})	1.29	2.52	2.95	0.30	0.80	3.01	1.77	2.52	2.97	0.50	2.02
$V\Omega_{6s_{1/2}\epsilon}$	−6.87	−2.94	−13.98	−0.59	−0.20	0.00	−7.47	−8.96	−11.92	−0.25	0.00
$V\Omega_{5d_{3/2}\epsilon}$	7.96	8.10	6.02	0.00	−0.49	2.55	6.12	8.96	5.99	−1.00	1.20

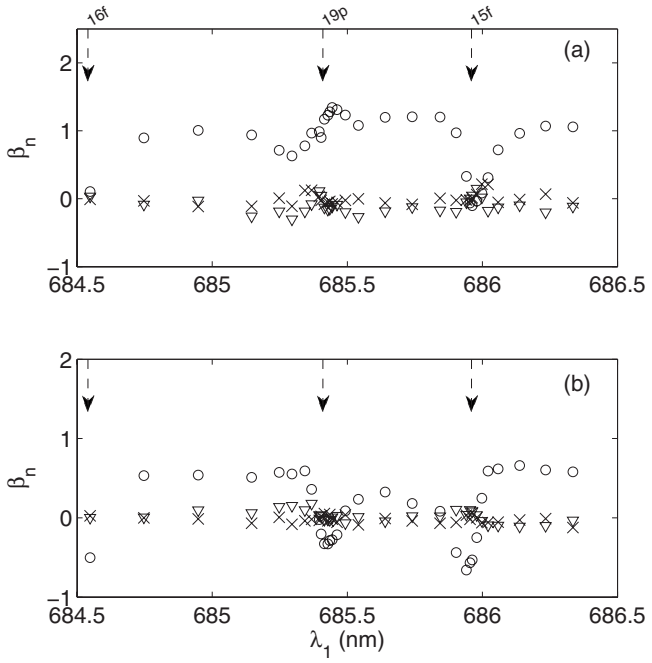

FIG. 6. PAD variation (variation in β_l) in the vicinity of the AIRs for the two-photon excitation by the red laser beam. The measured β_l are shown as a function of the red laser wavelength λ_1. The components shown are β_2 (○), β_4 (▽), and β_6 (×). In (a), we show the angular distribution components for the fast-electron signal, while in (b) we have the slow-electron terms. Strong variation in the PAD was observed near the AIR locations. Locations of $5d\,^2D_{5/2}nl[3/2]$ resonances are marked with dashed arrows at the top, with nl labeled.

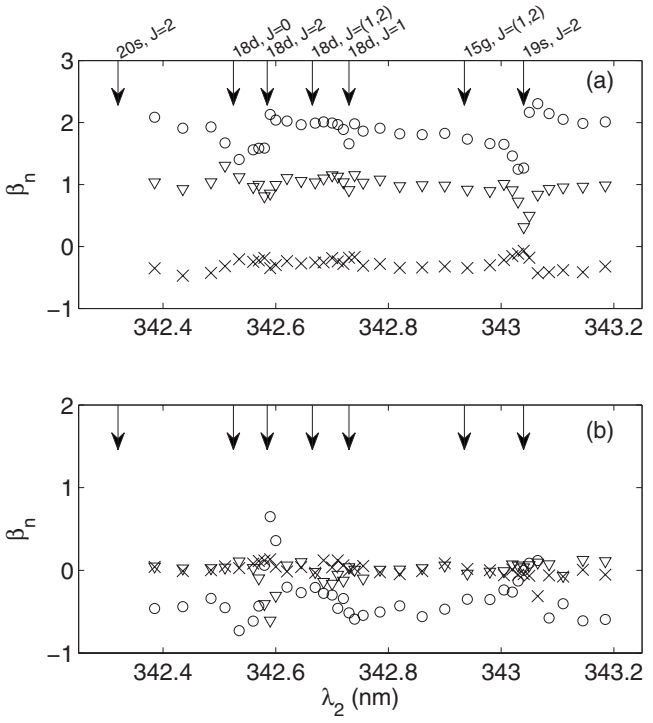

FIG. 7. PAD variation (variation in β_l) in the vicinity of the AIRs for the uv excitation. In (a), we show the angular distribution components for the fast-electron signal, while in (b) we have the slow-electron terms. Measured β_l are shown as a function of the uv laser wavelength λ_2. The components shown are β_2 (○), β_4 (▽), and β_6 (×). Locations of $5d\,^2D_{5/2}nl,J$ resonances are marked with solid arrows at the top, with nl and J labeled.

between the two excitation pathways. We show a set of typical images in Fig. 8. Figure 8(a1) shows a complete image, to which we apply appropriate masks to obtain the image containing only the fast electrons [Fig. 8(b1)] and mostly the slow electrons [Fig. 8(c1)]. We sum each of the columns of the complete and the masked images to form the traces shown in Figs. 8(a2), 8(b2), and 8(c2). The traces shown in subsequent rows of Fig. 8 [Figs. 8(a1)–8(c6)], obtained in a similar fashion, differ only in the relative optical phase $\Delta\phi$, and illustrate the changing image asymmetry. For example, we observe a variation in the asymmetry of the fast-electron images with $\Delta\phi$ by viewing the sequence of plots in Figs. 8(b2)–8(b6). In Fig. 8(b2), the fast-electron distribution is roughly symmetric, showing that the electrons are equally likely to go to the right or to the left. In Fig. 8(b3), however, the peak on the left is significantly larger than the peak on the right. In Fig. 8(b4), the peaks are again roughly the same, while in Fig. 8(b5) the electrons are more likely to move off to the right. Figure 8(b6) is again similar to Fig. 8(b3). Similarly, the series of plots in column (c) of Fig. 8 show the variation in the asymmetry of the slow-electron signal.

To quantify these asymmetries, we use a counting procedure very similar to that used to separate the yield for fast and slow electrons. We divide each image into its left and right halves, and sum the pixel values in each region to obtain the electron counts in the left half N_j^{left} and in the right half N_j^{right}. We define the asymmetry parameter as

$$\alpha_j^{asym} = \frac{N_j^{left}}{N_j^{left} + N_j^{right}}. \tag{2}$$

The fast electrons inside the slow electron regions *do show* a small asymmetry, which we account for when subtracting the fast-electron signal from the image before determining the left-right asymmetry for the slow electrons. We show a typical modulation in α_j^{asym} obtained from these images as a function of the optical phase difference $\Delta\phi$ in Fig. 9.

For each product channel, we fit the data with a sinusoidal function, offset from zero by a dc term, to obtain the phase in the asymmetry parameter. The phase difference between the two sinusoidal curves in these plots is defined as the phase lag $\Delta\phi_0$ between the two channels. Since the variation in the asymmetry parameter is small, typically less than 10% of the

TABLE III. Summary of possible outgoing electron waves, as obtained from the PAD observations.

Excitation	Parity	Channel	Outgoing electron waves
Red	Odd	$6s_{1/2}\epsilon$	Strong p wave
		$5d_{3/2}\epsilon$	Strong p wave
uv	Even	$6s_{1/2}\epsilon$	Strong d wave, occasional s wave near AIRs
		$5d_{3/2}\epsilon$	Almost always s wave

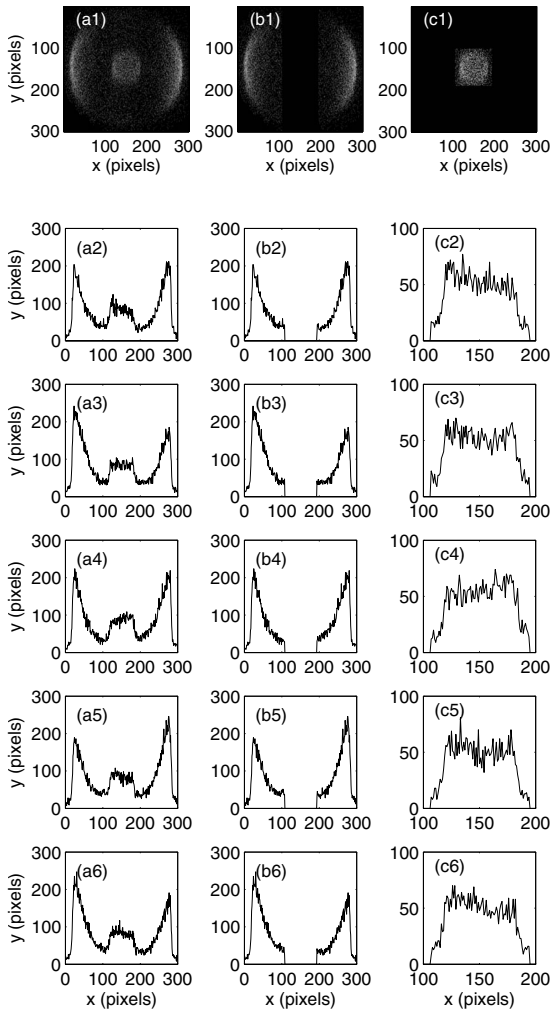

FIG. 8. Typical images recorded during the measurement of the asymmetric PAD. (a1) Raw data image; (b1) masked image for the fast-electron ($6s_{1/2}\epsilon$) signal; (c1) masked image for the slow-electron m signal. Traces (a2), (b2), and (c2) show the sum of each of the columns of the images from the top row. The sequence of data traces in rows (3)–(6) were collected with different optical phase differences $\Delta\phi$. The traces show clear variation in the left-right asymmetry for both fast and slow electrons.

total electron count, we repeated the measurement at each wavelength up to 15 times to reduce the uncertainty in $\Delta\phi_0$ to less than 7°.

We repeated the procedure at different laser wavelengths λ_1, and show the observed phase lag as a function of wavelength in Fig. 10. The phase lag shows a strong variation near both red and ultraviolet AIRs, confirming the critical role of these resonances. Our measurements covered the energy range slightly larger than $\Delta n=1$ of the autoionizing series. The phase lag (modulus 2π) is very similar at 684.8 and 686.2 nm, consistent with the repetitive patterns of similar resonance series. The data are relatively featureless in regions between resonances, and shows the largest variation of $\sim 2\pi$ near the $5d\,^2D_{5/2}15f[3/2]$ autoionizing resonance at the red wavelength of 685.9 nm. These data confirm the critical influence of these resonances on the phase lag for this system.

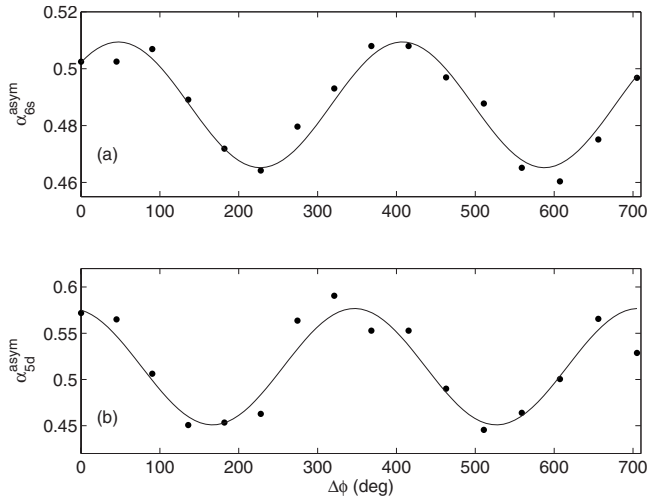

FIG. 9. Sinusoidal modulation observed in the asymmetry parameter α_j^{asym} for two channels, as defined in Eq. (2), as a function of the optical phase difference $\Delta\phi$. The line is the result of a least-squares fitting procedure. The phase difference between the two sinusoidal curves in these plots is defined as the phase lag $\Delta\phi_0$ between the two channels.

IV. DESCRIPTION OF THE PHASE LAG

Following the development and notation of Lambropoulos and Nakajima [5], we write the differential photoionization yield from an initial state $|i\rangle$ into a continuum channel $|\vec{k}_j\rangle=|c_j\rangle|\vec{k}\rangle$, where $|c_j\rangle$ $(j=1,2)$ denotes the residual ion state and $|\vec{k}\rangle$ the outgoing electron momentum state, in the following form:

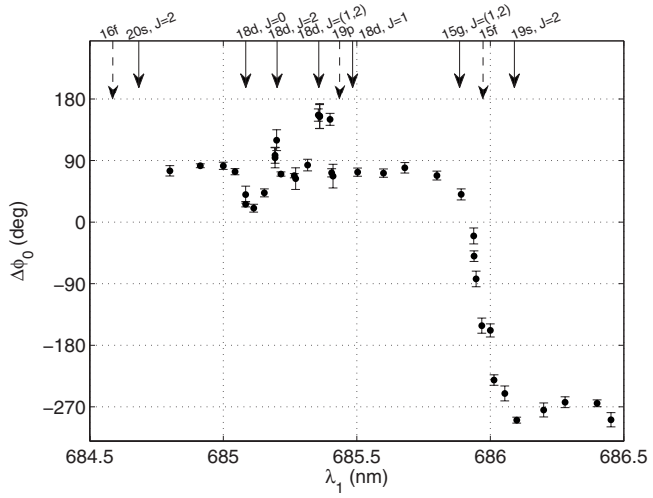

FIG. 10. Observed phase lag variation as a function of the red laser wavelength. Locations of $5d\,^2D_{5/2}nl[3/2]$ resonances are marked with dashed arrows at the top, while locations of $5d\,^2D_{5/2}nl,J$ resonances are marked with solid arrows. The variation in the phase lag is largest near the $5d\,^2D_{5/2}15f[3/2]$ autoionizing resonance, and the data are relatively featureless in regions between resonances. These data confirm the critical role of these resonances.

$$R_{\vec{k}_j}(\Theta,\Phi) = 2\pi \int dt\, f(t) \left| D^{(1)}_{\vec{k}_j i} e^{i\Delta\phi} + D^{(2)}_{\vec{k}_j i} + \sum_{n_1} \frac{V_{\vec{k}_j n_1} \Omega^{(1)}_{n_1} (1 - i/q_{n_1}) e^{i\Delta\phi}}{(\Delta_{n_1} + i\Gamma_{n_1}/2)} + \sum_{n_2} \frac{V_{\vec{k}_j n_2} \Omega^{(2)}_{n_2} (1 - i/q_{n_2})}{(\Delta_{n_2} + i\Gamma_{n_2}/2)} \right|^2 . \quad (3)$$

The quantities $D^{(M)}_{\vec{k}_j i}$ and $V_{\vec{k}_j n}$ represent the M-photon bound-free dipole matrix element coupling the initial state $|i\rangle$ to the $|\vec{k}_j\rangle$ continuum, and the matrix element of the configuration interaction coupling the resonant state $|n\rangle$ to the same continuum, respectively. Equation (3) differs from Eq. (1) and similar expressions in Ref. [5]. in the use of terms $D^{(M)}_{\vec{k}_j i}$ and $V_{\vec{k}_j n}$, rather than $D^{(M)}_{f,i}$ and $V_{f,n}$. The latter were introduced earlier to represent matrix elements coupling the initial state to final orbital angular momentum states $|f\rangle$ in the continuum, and are related to $D^{(M)}_{\vec{k}_j i}$ and $V_{\vec{k}_j n}$ through

$$D^{(M)}_{\vec{k}_j i}(\Theta,\Phi) = \sum_f \langle \vec{k}_j | f \rangle D^{(M)}_{fi},$$

$$V_{\vec{k}_j n}(\Theta,\Phi) = \sum_f \langle \vec{k}_j | f \rangle V_{fn}. \quad (4)$$

When two continua with different parities are excited coherently, the resultant photoelectron angular distribution forms an asymmetric distribution [16–22], which can be described in the form

$$R_{\vec{k}_j}(\Theta,\Phi) = S(\Theta,\Phi) + A(\Theta,\Phi)\cos(\Delta\phi + \phi^{(j)}_0), \quad (5)$$

where $S(\Theta,\Phi)$ and $A(\Theta,\Phi)$ represent the symmetric and antisymmetric components of the photoelectron angular distribution, respectively. The direction of the distribution asymmetry can be controlled by the optical phase difference $\Delta\phi$, while the phase lag of the asymmetric distribution for different products $j=1$ and 2 can be obtained as $\Delta\phi_0 = \phi^{(1)}_0 - \phi^{(2)}_0$.

From Eqs. (3) and (4), we see that two factors contribute to the phase lag for the asymmetric photoelectron angular distribution of this work. First, the channel phase, a term suggested in Ref. [5] for the phase difference resulting from the coupling between continuum channels through the discrete resonances, and calculated through determinations of q_n, $D^{(M)}_{fi}$, and V_{fn}, contributes. In total product state control (with ω-3ω interference, for example, where the two interfering pathways lead to the same final state continua), the phase lag $\Delta\phi_0$ comes solely from the channel phase [2,4,5]. For ω-2ω interference, however, observed through sinusoidal variations in the photoelectron angular distributions, the phase of the outgoing electronic waves also contributes to the phase lag. In order to illustrate this point, we write the final electron momentum state $|\vec{k}\rangle$ as [29]

$$|k\rangle = \sum_{l,m} 4\pi (i)^l e^{-i\xi_l} G_l(r) Y^*_{lm}(\Theta,\Phi) Y_{lm}(\theta,\phi)\chi_s, \quad (6)$$

where the phase of the outgoing wave is characterized by the free electron final orbital angular momentum quantum number l. The functions Y_{lm} are the spherical harmonics, the angular coordinates Θ and Φ represent the direction of the momentum of the photoelectron, while r, θ, and ϕ indicate the magnitude and direction of the electronic spatial position. The function χ_s represents the spin state of the photoelectron, whose projection along the quantization axis can be $\pm\hbar/2$. $G_l(r)$ is the radial part of the continuum wave function, which approaches $(|\vec{k}|r)^{-1}\sin[|\vec{k}|r + |\vec{k}|^{-1}\ln(2|\vec{k}|r) - l\pi/2 + \xi_l]$ for $|\vec{k}| \gg 1$. The asymptotic phase ξ_l of the continuum wave function can be written as the sum of two terms, the quantum-defect phase δ_l and the Coulomb phase η_l [30]. The phase of the final outgoing electron wave with orbital angular momentum of l, θ_l can be expressed as

$$\theta_l = \frac{\pi l}{2} - \xi_l = \frac{\pi l}{2} - (\eta_l + \delta_l). \quad (7)$$

Using Eq. (6) in Eqs. (4) allows us to write the matrix elements in a form that shows their explicit dependence on the phase of the outgoing electron wave θ_l,

$$D^{(M)}_{\vec{k}_j i}(\Theta,\Phi) = \sum_{l,m} Y_{lm}(\Theta,\Phi) \mathcal{D}^{(M)}_{lm,i} e^{-i\theta_l},$$

$$V_{\vec{k}_j n}(\Theta,\Phi) = \sum_{l,m} Y_{lm}(\Theta,\Phi) \mathcal{V}_{lm,n} e^{-i\theta_l}. \quad (8)$$

Substituting Eqs. (8) into Eq. (3), we can see that the channel phase and the phase of the outgoing electron wave each contribute to $\Delta\phi_0$. We present estimates of each of these contributions in the following section.

V. ANALYSIS

In this section, we present estimates of the channel phase and the phase lag due to the phase of the outgoing electronic wave in the wavelength range between 684.5 and 686.5 nm. It is not the intent of this work to calculate the exact phase of the outgoing waves nor the AIR structures, but rather to investigate the qualitative features of the phase lag variation. To this end, we estimate the phase lag variation, and show that (1) the two contributions are of comparable magnitude and therefore both important, and (2) their strongest variations occur near discrete resonances, one near the uv single-photon resonances, the other near the two-photon red resonances.

A. Estimated phase lag variation due to the autoionizing resonance structures

We estimate the channel phase using the parameters that describe the relative intensity and asymmetric line shapes of the autoionizing spectra shown in Fig. 5. We listed these parameters in Tables I and II. We calculate the expected phase lag in this spectra region using Eq. (3), setting the phase of the electron outgoing waves equal to zero. The re-

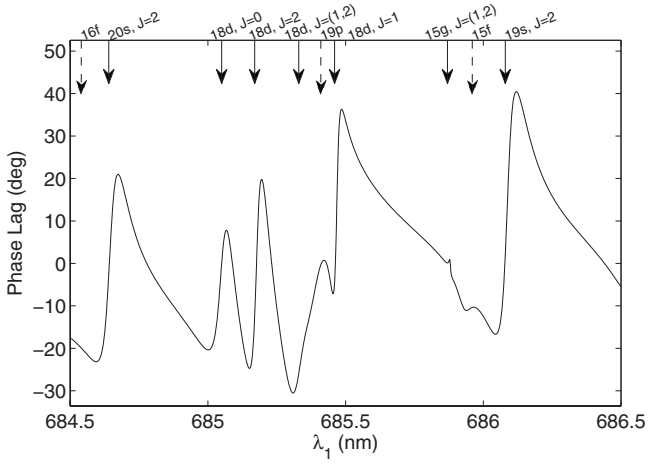

FIG. 11. Resulting phase lag between the two photoionization channels calculated using the autoionizing parameters presented in Tables I and II. Locations of $5d\,^2D_{5/2}nl[3/2]$ resonances are marked with dashed arrows at the top, while locations of $5d\,^2D_{5/2}nl,J$ resonances are marked with solid arrows.

sults should, therefore, reflect only the channel phase, i.e., the phase lag variation due to the phase change in the transition moments through the resonance structures. We show the result of this calculation in Fig. 11. The calculated phase lag shows clear variation across the resonance structures. The maximum variation in the phase lag across any resonance is about 60°. Our estimates show that the channel phase varies much more rapidly near ultraviolet AIRs than it does near the red AIR peaks, consistent with expectations based upon the theoretical formulation of Lambropoulos and Nakajima [5], who predicted rapid variation of the channel phase near AIR structures for which the Fano asymmetry parameter q is small. Small q indicates that the direct coupling and the coupling through the autoionizing resonance to the continuum are of comparable strength. In our experiment, the peak heights of the ultraviolet AIRs were much smaller than for the red two-photon spectra, and the q parameters smaller, making strongly interfering spectra as shown in the previous section. In contrast, the red AIR peaks were much larger than the corresponding ultraviolet resonances and nearly symmetric in line shape. At these resonances, the strong transitions through the autoionizing resonances dominate the direct coupling to the continuum, and interferences play a less important role. Therefore, the channel phase does not show much variation near the red AIRs.

B. Estimated phase lag variation due to the outgoing electron waves

In order to estimate the phase lag variation due to the outgoing electron waves, we must estimate (1) the relative amplitudes of the different outgoing partial waves, and (2) the phase difference between different outgoing partial waves. In the following, we present our estimates of the relative amplitudes and phases of these partial waves, as well as our estimate of their overall contribution to the phase lag.

TABLE IV. The phase difference between different outgoing waves (in radians).

	Final channel	
	$6s_{1/2}\epsilon$	$5d_{3/2}\epsilon$
$\theta_s-\theta_p$	−4.12	−4.59
$\theta_s-\theta_f$	−20.98	−20.68
$\theta_d-\theta_p$	5.84	6.24
$\theta_d-\theta_f$	−11.01	−9.85

From the PAD measurement for each excitation pathway, we estimate the major components for the outgoing waves to be s and d waves for the even-parity channel (via uv excitation) and mostly p waves for the odd-parity channel (via red excitation). We estimate the number of electrons N_l coupled to each outgoing wave with orbital angular momentum l, from the β_l values displayed in Figs. 6 and 7.

We also estimate the phase difference between the final waves using Eq. (7), and list these terms in Table IV. We calculated the Coulomb phase difference $\eta_l-\eta_{l'}$ from the kinetic energy of the photoelectron, as discussed in Appendix A. We obtained estimates of the quantum defect phase δ_l of the continuum partial waves from the energies of bound state spectra for even- and odd-parity J states [31–35]. Details of the parameters used for the determination of the quantum defect phase are compiled in Appendix B. The variation in the quantum defect μ_l for different J states was less than 10% and we used the average value of μ_l to calculate the quantum defect phase $\delta_l=\pi\mu_l$. The Coulomb phase, quantum defect phase, and $\pi l/2$ phase were all added to calculate the phase difference between different outgoing waves.

Using the N_l and θ_l values, the asymmetry parameter α_j^{asym} due to the PAD interference between even- and odd-parity electron waves has the form

$$\alpha_j^{asym}(\Delta\phi)=\sqrt{N_l^jN_{l'}^j}\,\cos(\Delta\phi+\theta_l^j-\theta_{l'}^j)+\text{const}, \qquad (9)$$

where l and l' are the orbital angular momenta for even and odd outgoing electron waves with the corresponding phases θ_l and $\theta_{l'}$, respectively. By casting the equation above in the form of the second term in the right-hand side of Eq. (5), the phase $\phi_0^{(j)}$ of each channel can be expressed as

$$\phi_0^{(j)}=\arctan\left(\frac{\sum_{ll'}\sqrt{N_l^jN_{l'}^j}\,\sin(\theta_l^j-\theta_{l'}^j)}{\sum_{ll'}\sqrt{N_l^jN_{l'}^j}\,\cos(\theta_l^j-\theta_{l'}^j)}\right), \qquad (10)$$

where the summation in l and l' is added to account for multiple outgoing waves. We calculate the phase lag variation expected from the N_l and the outgoing electron phase θ_l for each channel with Eq. (10), and show the result in Fig. 12.

The calculated phase shows a strong variation for both the fast- and slow-electron channels, especially near even-parity AIRs. At 685.4 and 685.95 nm, there are red autoionizing resonances ($5d_{5/2}19p$ and $5d_{5/2}15f$ resonances, respectively), where the outgoing wave from the red excitation changes

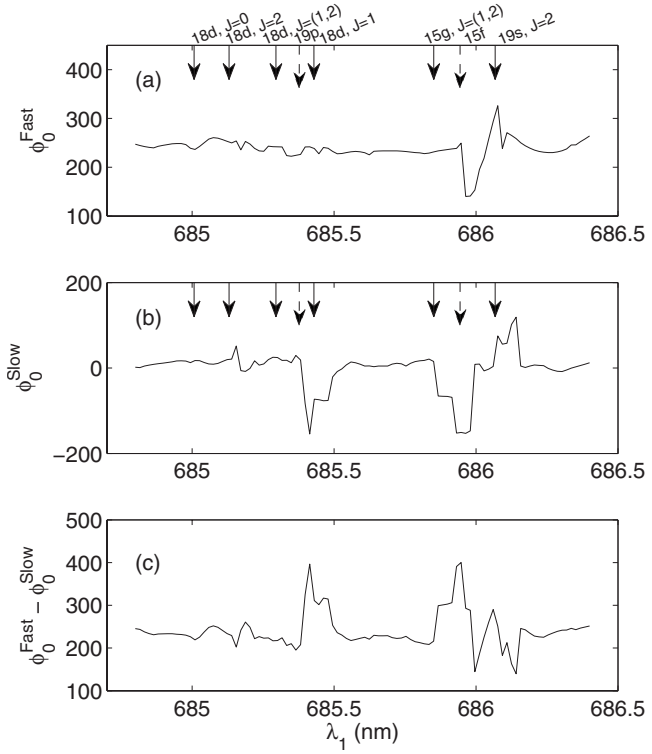

FIG. 12. Calculated phase lag due to the variation of the outgoing electron waves. First row, ϕ_0 variation for the fast-electron channel; second row, ϕ_0 variation for the slow-electron channel; third row, $\Delta\phi_0$ variation. The variation of the phase lag was calculated to be as large as 210°.

strongly. Phase lag variations of up to 200° can be seen near these AIRs. There is a smaller variation in the phase of around 50° at 686.1 nm, near the ultraviolet excitation AIRs. As a result, the phase lag variation between the two channels shows strong variation near the red AIRs. The largest variation is around 210°. There are some variations due to the ultraviolet AIRs, but the effect is limited to less than 100° for those AIRs. These estimates are consistent with the conclusions of Keller *et al.* [28], who previously reported on the variation of the photoelectron angular distributions in the vicinity of autoionizing resonances. They observed large PAD variations near symmetric peaks in their study, and small variations near asymmetric peaks. The strong variation in the PAD near symmetric peaks was explained as follows. One expects that the outgoing electronic wave excited through the direct coupling to the continuum state is in general different from the outgoing wave excited through the autoionizing resonance. Near large, symmetric peaks embedded in the continuum, therefore, the outgoing wave is very different when the laser is on resonance from that when the laser is tuned away from resonance. By contrast, near smaller asymmetric peaks, the variation in the outgoing wave is not nearly as complete when tuning the laser through resonance, since the electronic wave excited when the laser is resonant has comparable components of the direct wave and the discrete resonance-mediated wave.

VI. DISCUSSION AND CONCLUSION

Experimentally, we have measured the phase lag for ω-2ω interference, resulting in asymmetric photoelectron angular distributions. We observe rapid variation of the phase lag near two-photon (red) and uv resonances, with the largest effect near a two-photon (red) resonance. Additionally, we have shown our estimate of the phase lag variation due to two separate effects; the channel phase, due to the autoionizing resonance structures; and the phase of the electron outgoing waves.

These two separate effects seem to be important near different sets of AIRs. The strong asymmetry in the uv-excited AIR peaks implies strong interference between two different couplings to the continuum. It also implies that the strong interference takes place since the outgoing electron waves for two couplings are similar, therefore the phase lag variation due to the outgoing electron waves should be small for these resonances. Conversely, near the red-laser-excited two-photon AIR peaks, the phase of the outgoing electronic wave seems to play the dominant role.

The magnitude of the variation of the phase lag was found to be larger, in the case we have studied, for the variation in the electron outgoing waves than for the channel phase. The maximum phase lag variations calculated for the two effects were about 60° and 210° due to the resonance effect and the outgoing waves, respectively. From these numbers the largest variation possible by simply summing two effects can be 270°, while our experiment shows a larger variation of over 2π. In the experiment, the two effects discussed are not separable and the measured phase lag variation should include both of these effects simultaneously. While our simple model estimates of the phase lag variation due to channel and electronic phases show many of the qualitative features that we observe in our experiment, we hope that this work will stimulate more precise calculations of the phase lag in this system.

In conclusion, we observed a large variation of the phase lag in the asymmetric photoelectron angular distribution. A large phase lag variation of over 2π was observed. Additionally, we performed a spectroscopic study of the AIRs in the vicinity as well as the PAD variation near those AIRs. Our analysis clearly shows the strong impact of the resonance effect in the phase lag variation; however, quantitative agreement could not be achieved with our simple model and further oncoming investigations from the theorists will be necessary for a detailed understanding of these effects. Nonetheless, our study demonstrates the variation of the phase lag in a simple system, where the resonance structures are well resolved and well studied, forming a basis for tests of the current and future theory.

ACKNOWLEDGMENT

This material is based upon work supported by the National Science Foundation under Grant No. 0099477.

APPENDIX A: COULOMB PHASE DIFFERENCE CALCULATION

The Coulomb phase is of the form $\eta_l = \arg\{\Gamma(l+1 - i/\sqrt{\epsilon})\}$ where Γ is the complex gamma function and ϵ is the

TABLE V. Coulomb phase difference for different combinations of outgoing electron waves (in radians). Electron kinetic energy ϵ used for the calculation was 0.0476 and 0.0032 Ry for $6s_{1/2}\epsilon$ and $5d_{3/2}\epsilon$ electrons, respectively.

	Final channel	
	$6s_{1/2}\epsilon$	$5d_{3/2}\epsilon$
$\eta_s-\eta_p$ (rad)	1.36	1.51
$\eta_s-\eta_f$ (rad)	3.51	4.38
$\eta_d-\eta_p$ (rad)	−1.16	−1.46
$\eta_d-\eta_f$ (rad)	0.99	1.40

kinetic energy of the electron in rydbergs. We utilize a factorial expansion of the gamma function:

$$\Gamma(z) = (z-1)\,!\,. \tag{A1}$$

For $\eta_s-\eta_f$ ($l=0$ and 3 for s and f waves, respectively),

$$\eta_s-\eta_f = \arg\{\Gamma(1-i/\sqrt{\epsilon})\} - \arg\{\Gamma(4-i/\sqrt{\epsilon})\} = \arctan\left(\frac{1}{\sqrt{\epsilon}}\right) + \arctan\left(\frac{1}{2\sqrt{\epsilon}}\right) + \arctan\left(\frac{1}{3\sqrt{\epsilon}}\right). \tag{A2}$$

Similarly,

TABLE VI. List of quantum defect parameters for different outgoing electron channels. Parameters with an asterisk were not listed in the reference. The value on the chart is used for the calculation.

Excitation laser/parity	jj	J	μ_0	μ_1
uv/even	$6s_{1/2}ns_{1/2}$	$6sns\ ^1S_0$	4.1817	0.3981
	$5d_{3/2}nd_{3/2}$	$5dnd\ ^3P_0$	2.6185	0
uv/even	$6s_{1/2}nd_{3/2}$	$6snd\ ^3D_2$	2.7668	1.034
	$6s_{1/2}nd_{5/2}$	$6snd\ ^1D_2$	2.7312	2.014
	$5d_{3/2}ns_{1/2}$	$5dns\ ^3D_2$	4.1818	0.366
	$5d_{3/2}nd_{3/2}$	$5dnd\ ^3D_2$	2.8015	0.8
	$5d_{3/2}nd_{5/2}$	$5dnd\ ^3F_2$	2.6191	1
Red/odd	$6s_{1/2}np_{1/2}$	$6snp\ ^3P_0$	3.819	0.36
	$5d_{3/2}np_{3/2}$	$5dnp\ ^3P_0$	3.657	0*
Red/odd	$6s_{1/2}np_{1/2}$	$6snp\ ^3P_1$	3.808	0.27
	$6s_{1/2}np_{3/2}$	$6snp\ ^1P_1$	3.791	0.198
	$5d_{3/2}np_{1/2}$	$5dnp\ ^3D_1$	3.702	0.303
	$5d_{3/2}np_{3/2}$	$5dnp\ ^3P_1$	3.699	0.071
	$5d_{3/2}nf_{5/2}$	$5dnf\ ^1P_1$	0.503	−0.293
Red/odd	$6s_{1/2}nf_{5/2}$	$6snf\ ^3F_2$	0.184	0*
	$6s_{1/2}np_{3/2}$	$6snp\ ^3P_2$	3.785	0*
	$5d_{3/2}np_{3/2}$	$5dnp\ ^3D_2$	3.726	0*
Red/odd	$6s_{1/2}nf_{7/2}$	$6snf\ ^1F_3$	0.144	−1
	$6s_{1/2}nf_{5/2}$	$6snf\ ^3F_3$	0.185	−1
	$5d_{3/2}np_{3/2}$	$5dnp\ ^3F_3$	3.716	0

$$\eta_s-\eta_p = \arctan\left(\frac{1}{\sqrt{\epsilon}}\right), \tag{A3}$$

$$\eta_d-\eta_p = -\arctan\left(\frac{1}{2\sqrt{\epsilon}}\right), \tag{A4}$$

$$\eta_d-\eta_f = \arctan\left(\frac{1}{3\sqrt{\epsilon}}\right). \tag{A5}$$

We used $\epsilon=0.0476$ and 0.0032 Ry for the kinetic energy of fast and slow electrons, respectively. Calculated Coulomb phase differences for different combinations of outgoing electron waves are tabulated in Table V.

APPENDIX B: QUANTUM DEFECT PHASE

The quantum defect phase δ_l for each electron wave is of the form $\delta_l(\epsilon)=\pi\mu_l(\epsilon)$ where $\mu_l(\epsilon)$ is the quantum defect of the l outgoing wave at ϵ.

The quantum defect parameters used to calculate the quantum defect phase for each outgoing wave are listed in Table VI. We interpolated μ_l to energy ϵ using a linear equation,

$$\mu_l = \mu_0 + \mu_1\epsilon, \tag{B1}$$

where ϵ is the kinetic energy of the outgoing electron wave in rydbergs used in the previous section.

The calculated quantum defect phases as well as the average quantum defects used for the calculation are listed in Table VII.

Using Eq. (7), the total phase differences between different outgoing waves were calculated. The results are tabulated in Table IV.

TABLE VII. Average quantum defect and the quantum defect phase calculated from the average quantum defect for different outgoing waves.

Even-parity channels				
	$6s_{1/2}\epsilon$		$5d_{3/2}\epsilon$	
Outgoing wave	s	d	s	d
μ_l	4.20	2.83	4.18	2.68
δ_l (rad)	13.19	8.89	13.13	8.42
Odd-parity channels				
	$6s_{1/2}\epsilon$		$5d_{3/2}\epsilon$	
Outgoing wave	p	f	p	f
μ_l	3.81	0.14	3.70	0.49
δ_l (rad)	11.97	0.44	11.62	1.54

[1] L. Zhu, V. Kleiman, X. Li, S. P. Lu, K. Trentelman, and R. J. Gordon, Science **270**, 77 (1995).
[2] L. Zhu, K. Suto, J. A. Fiss, R. Wada, T. Seideman, and R. J. Gordon, Phys. Rev. Lett. **79**, 4108 (1997).
[3] A. Khachatrian, R. Billoto, L. Zhu, R. J. Gordon, and T. Seideman, J. Chem. Phys. **116**, 9326 (2002).
[4] J. A. Fiss, L. Zhu, R. J. Gordon, and T. Seideman, Phys. Rev. Lett. **82**, 65 (1999).
[5] P. Lambropoulos and T. Nakajima, Phys. Rev. Lett. **82**, 2266 (1999).
[6] H. Lefebvre-Brion, J. Chem. Phys. **106**, 2544 (1997).
[7] T. Nakajima, J. Zhang, and P. Lambropoulos, J. Phys. B **30**, 1077 (1997).
[8] A. Lyras and H. Bachau, Phys. Rev. A **60**, 4781 (1999).
[9] S. Lee, J. Chem. Phys. **108**, 3903 (1998).
[10] T. Seideman, J. Chem. Phys. **108**, 1915 (1998).
[11] T. Seideman, J. Chem. Phys. **111**, 9168 (1999).
[12] A. Apalategui, A. Saenz, and P. Lambropoulos, Phys. Rev. Lett. **86**, 5454 (2001).
[13] R. Yamazaki and D. S. Elliott, Phys. Rev. Lett. **98**, 053001 (2007).
[14] K. Maeda, K. Ueda, M. Aymar, T. Matsui, H. Chiba, and K. Ito, J. Phys. B **33**, 1943 (2000).
[15] P. Camus, M. Dieulin, A. El Himdy, and M. Aymar, Phys. Scr. **27**, 125 (1983).
[16] Y.-Y. Yin, C. Chen, D. S. Elliott, and A. V. Smith, Phys. Rev. Lett. **69**, 2353 (1992).
[17] Yi-Yian Yin, D. S. Elliott, R. Shehadeh, and E. R. Grant, Chem. Phys. Lett. **241**, 591 (1995).
[18] B. Sheehy, B. Walker, and L. F. DiMauro, Phys. Rev. Lett. **74**, 4799 (1995).
[19] E. Dupont, P. B. Corkum, H. C. Liu, M. Buchanan, and Z. R. Wasilewski, Phys. Rev. Lett. **74**, 3596 (1995).
[20] A. Haché, Y. Kostoulas, R. Atanasov, J. L. P. Hughes, J. E. Sipe, and H. M. van Driel, Phys. Rev. Lett. **78**, 306 (1997); H. M. van Driel, J. E. Sipe, A. Haché, and R. Atanasov, Phys. Status Solidi B **204**, 3 (1997).
[21] T. Nakajima, Phys. Rev. A **61**, 041403(R) (2000).
[22] H. Ohmura, T. Nakanaga, and M. Tachiya, Phys. Rev. Lett. **92**, 113002 (2004).
[23] D. W. Schumacher, F. Weihe, H. G. Muller, and P. H. Bucksbaum, Phys. Rev. Lett. **73**, 1344 (1994).
[24] H. Helm, N. Bjerre, M. J. Dyer, D. L. Huestis, and M. Saeed, Phys. Rev. Lett. **70**, 3221 (1993).
[25] R. Yamazaki and D. S. Elliott, Phys. Rev. A **73**, 023415 (2006).
[26] Z.-M. Wang and D. S. Elliott, Phys. Rev. A **62**, 053404 (2000).
[27] C. Bordas, F. Paulig, H. Helm, and D. L. Huestis, Rev. Sci. Instrum. **67**, 2257 (1996).
[28] J. S. Keller, J. E. Hunter, and R. S. Berry, Phys. Rev. A **43**, 2270 (1991).
[29] P. Lambropoulos and M. R. Teague, J. Phys. B **9**, 587 (1976).
[30] A. Burgess and M. J. Seaton, Mon. Not. R. Astron. Soc. **120**, 121 (1960).
[31] M. Aymar, P. Camus, M. Dieulin, and C. Morillon, Phys. Rev. A **18**, 2173 (1978).
[32] M. Aymar and O. Robaux, J. Phys. B **12**, 531 (1979).
[33] J. A. Armstrong, J. J. Wynne, and P. Esherick, J. Opt. Soc. Am. **69**, 211 (1979).
[34] B. H. Post, W. Vasen, W. Hogervorst, M. Aymar, and O. Robaux, J. Phys. B **18**, 187 (1985).
[35] M. C. Baruch, L. Cai, R. R. Jones, and T. F. Gallagher, Phys. Rev. A **45**, 6395 (1992).